Global Estimates for High-Spatial-Resolution Clear-Sky Land Surface Upwelling Longwave Radiation From MODIS Data

Jie Cheng, *Member, IEEE*, and Shunlin Liang, *Fellow, IEEE*

Abstract—Surface upwelling longwave radiation (LWUP) is a vital component in calculating the Earth's surface radiation budget. Under the general framework of the hybrid method, we developed linear and dynamic learning neural network (DLNN) models for estimating the global 1-km instantaneous clear-sky LWUP from the top-of-atmosphere radiance of Moderate Resolution Imaging Spectroradiometer thermal infrared channels 29, 31, and 32. Extensive radiative transfer simulations were conducted to produce a large number of representative samples, from which the linear model and DLNN model were derived. These two hybrid models were evaluated using ground measurements collected at 19 sites from three networks (SURFRAD, ASRCOP, and GAME-AAN). According to the validation results, the linear model was more accurate than the DLNN model, with a bias and root-mean-square error (RMSE) of -0.31 W/m^2 and 19.92 W/m^2 obtained by averaging the mean bias and RMSE for the three networks. Additionally, the computational efficiency of the linear model was much higher than that of the DLNN model. We also compared our linear model to a hybrid method developed by a previous study and found ours to perform better.

Index Terms—Moderate Resolution Imaging Spectroradiometer (MODIS), remote sensing, surface radiation budget (SRB), surface upwelling longwave radiation (LWUP).

I. INTRODUCTION

SURFACE upwelling longwave radiation (LWUP) (4–100 μm) is one of the four components required to calculate the Earth's surface radiation budget (SRB), which is central to land surface models that characterize the planet's hydrological, ecological, and biogeochemical processes [1]–[3]. LWUP is also an indicator of the Earth's surface temperature as well as a diagnostic parameter for numerical weather prediction models.

Remote sensing is the unique means of estimating regional and global LWUP. Currently, there are three widely used satellite-derived data sets of longwave radiation: the Global Energy and Water cycle Experiment-Surface Radiation Budget (GEWEX-SRB), the International Satellite Cloud Climatology Project-Flux Data (ISCCP-FD), and the Clouds and the Earth's Radiant Energy System-Gridded Radiative Fluxes and Clouds (CERES-FSW). The accuracy of these three data sets varies from 21 to 33.6 W/m^2 at the monthly timescale and at a 100–280-km spatial resolution [4]. Gui *et al.* collected the ground measurements at 15 sites in four regions (North America, Southeast Asia, the Qinghai-Tibetan, and Japan) of different climate and land-cover types to evaluate the accuracy of the aforementioned three longwave flux data sets [5]. The bias of all-sky LWUP ranges from -4.2 to 6.9 W/m^2, and the root-mean-square error (RMSE) ranges from 22.7 to 31.5 W/m^2. The bias lies between -3.8 and 11.3 W/m^2, and the RMSE lies between 21 and 23 W/m^2 for clear-sky LWUP. The meteorological, hydrological, and agricultural research communities require an accuracy of 5–10 W/m^2 for LWUP retrieved from satellite data at a 25–100-km spatial resolution and 3-h daily temporal resolution [6]. The acceptable accuracy for satellite-derived instantaneous LWUP is 20 W/m^2 [7]. Clearly, current satellite LWUP and longwave flux products cannot meet the requirements of users. Another drawback of these three longwave flux data sets is their coarse spatial resolutions. High-spatial-resolution longwave fluxes (down to 1 km) are important diagnostic parameters for mesoscale land surface and atmosphere models, particularly over heterogeneous areas [8], [9]. Additionally, high-spatial-resolution LWUP can serve as a medium scale for the validation of coarse resolution data, as LWUP varies on much finer spatial scales [10].

Usually, we have two methods to estimate high-spatial-resolution LWUP from satellite observations. One is the temperature–emissivity method [11], [12], which directly calculates LWUP using satellite-derived land surface temperatures (LSTs), broad-band emissivity (BBE), and surface downwelling longwave radiation (LWDN), such as the Moderate Resolution Imaging Spectroradiometer (MODIS) LST product [13] and the Global Land Surface Satellite BBE product [14], [15]. The other is called the hybrid method, which links the LWUP to satellite top-of-atmosphere (TOA) radiance or brightness temperature (BT) by extensive radiative transfer simulation and statistical analysis [12], [16]. It is convenient to estimate LWUP using the temperature–emissivity method because there are many algorithms for retrieving LST and emissivity [11], [17], [18]. However, current satellite LST and emissivity products have large uncertainties [19]–[21]. As a

J. Cheng is with the State Key Laboratory of Remote Sensing Science, School of Geography, Beijing Normal University, Beijing 100875, China (e-mail: brucechan2003@126.com).

S. Liang is with the State Key Laboratory of Remote Sensing Science, School of Geography, Beijing Normal University, Beijing 100875, China, and also with the Department of Geographical Science, University of Maryland, College Park, MD 20742 USA.
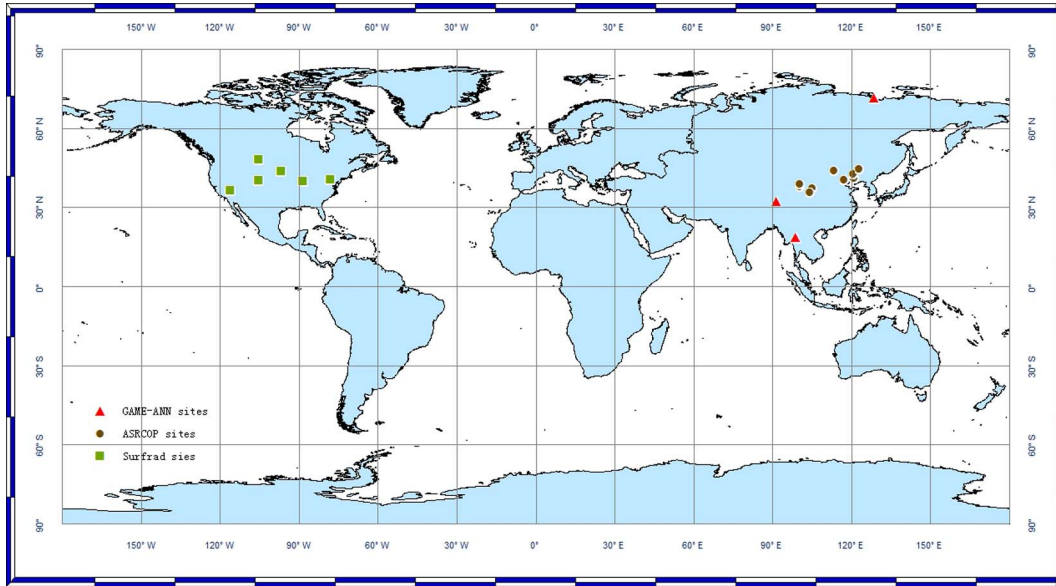
Fig. 1.   Distribution of 19 validation sites in this paper.

result, we cannot achieve high accuracy when estimating LWUP with this method [12]. The hybrid method was primarily used to estimate LWDN [22]–[24]. The advantage of this method is that it bypasses the problem of separating the LST and emissivity so that a more accurate estimation of the LWUP can be achieved. Wang *et al.* pioneered the study of estimating high-spatial-resolution land surface LWUP and LWDN [4], [12], [25]. Wang *et al.* evaluated the accuracy of the temperature–emissivity and hybrid methods at six SURFRAD sites using MODIS LST, BBE derived from MODIS narrow-band emissivities, and ground-measured LWDN [10]. Their work indicated that the accuracy of the temperature–emissivity method is much lower than that of the hybrid method. For the former method, the bias ranges from -13.63 to -27.14 W/m^2, and the RMSE ranges from 16.55 to 28.09 W/m^2; for the latter method, the bias ranges from -4.53 to -16.41 W/m^2, and the RMSE ranges from 11.79 to 18.70 W/m^2. The hybrid method has consequently gained popularity for the estimation of high-spatial-resolution LWUP from satellite data [16], [26]. However, the questions of whether this method can be adapted from the regional scale to the global scale-and what accuracy might then be achieved-remain unanswered.

The purpose of this paper was to estimate the high-quality global 1-km instantaneous clear-sky LWUP from MODIS data using the general framework of the hybrid method. The rest of this paper is arranged as follows. Section II describes the data used in this paper. Section III describes the methods, followed by the evaluation of results and discussion, and the conclusions are given in Section V.

II. DATA

A. Satellite Data

The Atmospheric Infrared Sounder (AIRS) is an infrared grating spectroradiometer on board the National Aeronautics and Space Administration polar platform Aqua [27]. AIRS measures high spectral resolution ($v/\Delta v = 1200$) radiation emitted by the Earth's surface and atmosphere within the spectral range of 3.7–15.4 μm, from which the level-2 AIRS standard product (the cloud and surface properties as well as the profiles of retrieved temperature, water vapor, ozone, carbon monoxide, and methane) was derived [28]. The temperature profile has 28 levels in total, with the corresponding pressure varying from 1100 to 0.1 mb, while the water vapor profile is reported to have 14 layers, with pressure ranging from 1100 to 50 mb. The spatial resolution of the AIRS L2 standard product is 0.05°. Two years (2007–2008) of AIRS L2 standard temperature and water vapor profiles were used to construct the atmosphere profile database in this paper.

The MODIS can provide accurate high-spatial-resolution land, ocean, and atmosphere products from at least four daily observations over most locations on the Earth's surface. The MODIS TOA radiance product MOD021KM and MODIS cloud product MOD35 were used as inputs to the hybrid method for estimating clear-sky LWUP. During the validation, the MODIS geolocation product MOD03 was used to find the matchup.

B. Ground Measurements

Ground-measured LWUP data collected at 19 sites from three independent networks were used to evaluate the estimated LWUP in this paper. Fig. 1 shows the distribution of sites. Table I summarizes the latitude, longitude, elevation, land cover, and period of observation time.

1) SURFRAD: NOAA's Office of Global Programs established SURFRAD in 1993. SURFRAD data have been acquired for grassland, cropland, and desert land-cover types and widely used for satellite-derived land surface and atmospheric product validation. LWUP was measured by the Precision Infrared

TABLE I
DESCRIPTION OF SITE CONDITIONS

Name	Latitude (°)	Longitude (°)	Elevation (m)	Land cover	Time period
Bondville[a]	40.05 N	88.37 W	213	Cropland	2003-2005
Boulder[a]	40.13 N	105.24 W	1689	Grassland	2003-2005
Desertrock[a]	36.63 N	116.02 W	1007	Desert	2003-2005
Fortpeck[a]	48.31 N	105.10 W	634	Grassland	2003-2005
Pennstate[a]	40.72 N	77.93 W	376	Cropland	2003-2005
Siouxfalla[a]	43.73 N	96.62 W	473	Grassland	2003-2005
Arou[b]	38.04 N	100.47 E	3033	Desert/grassland	2008-2008
Dongsu[b]	44.09 N	113.57 E	970	Desert/grassland	2008-2009
Jingzhou[b]	41.18 N	121.21E	22	Cropland	2008-2009
Miyun[b]	40.63 N	117.32 E	350	Cropland	2008-2008
Naiman[b]	42.93 N	120.70 E	361	Desert/ oasis	2008-2008
Shapotou[b]	37.32 N	105.11 E	1227	Desert	2008-2008
Tongyu grass[b]	44.57 N	122.92 E	184	Grassland	2008-2009
Tongyu crop[b]	44.59 N	122.93 E	184	Cropland	2008-2009
Yingke[b]	38.86 N	100.41 E	1519	Cropland/oasis	2008-2008
Yuzhong[b]	35.95 N	104.13 E	1965	Desert/grassland	2008-2009
Amdo[c]	32.24 N	91.62 E	4700	Desert/grassland	2000-2003
Kogma[c]	18.81 N	98.90 E	1268	Forest	2000-2001
Tiksi[c]	71.59 N	128.77 E	40	Shrubland	2000-2002

[a]SURFRAD sites; [b]ASRCOP sites; [c]GAME-AAN sites

Radiometer (model PIR, Eppley Laboratories) in the spectral range of 3–50 μm. The PIRs are mounted ~8 m above the ground, and the maximum signal comes from a 45° viewing zenith angle. SURFRAD has three standard PIRs calibrated annually at the World Radiation Center's Physikalisch-Meteorologisches Observatorium in Davos (PMOD), Switzerland. After the SURFRAD standard, PIRs are calibrated in the blackbody, and their calibrations are fine-tuned by running them outdoors against PMOD's World Pyranometer Standard Group. Field instruments are calibrated in operation next to the three standard PIRs, using the simultaneous data to transfer the mean calibration of the three standard PIRs to each field instrument. During daytime, a shade ball shades the PIR dome to minimize errors associated with inward infrared emission from the dome to the thermopile. Albrecht and Cox's method is used to correct for dome emission and to compute the longwave irradiance [29]. The overall accuracy of ground data is approximately ±9 W/m^2 [30]. LWUP measurements are 3-min averaged values that are distributed in near real time by anonymous FTP and the WWW (http://www.srrb.noaa.gov). Data from six sites were downloaded and used to validate the hybrid method in this paper.

2) ASRCOP: The Arid and Semi-arid Region Collaborative Observation Project (ASRCOP) provides pyranometer data from 18 China meteorological sites in the summers of 2008 and 2009 [31], [32]. All of the instruments were collectively calibrated by ASRCOP in June 2008. The ASRCOP LWUP was recorded with a temporal resolution of 30 min. Data from ten sites were used after excluding the sites with questionable or discontinuous observations.

3) GAME-AAN: The Asian Automatic Weather Station Network (AAN), supported by the Global Energy and Water

Cycle Experiment (GEWEX) Asian Monsoon Experiment (GAME-AAN), was implemented to understand the role of the Asian monsoon in the global energy and water cycles. GAME-AAN provided LWUP measurements at sites with a temporal resolution of 30 min. Information on the sensor and measurement accuracies is available at the website (http://aan.suiri.tsukuba.ac.jp). Three sites with LWUP measurements after year 2000 were selected to validate the hybrid method in this paper.

III. METHOD

Discounting the scattering of thermal infrared radiation, the clear-sky radiance measured by thermal infrared sensors can be approximated as

$$B_i(T_i) = \varepsilon_i B_i(T_s)\tau_i(\theta, \varphi, P_s \to 0)$$

$$+ \int_{P_s}^{0} B_i(T_p)\frac{d\tau_i(\theta, \varphi, P_s \to 0)}{d\ln P}d\ln P$$

$$+ \frac{(1-\varepsilon_i)}{\pi}\int_{0}^{2\pi}\int_{0}^{\frac{\pi}{2}}\int_{P_s}^{0} B_i(T_p)\frac{d\tau_i(\theta', \varphi'P \to P_s)}{d\ln P}$$

$$\times \cos\theta'\sin\theta'd\ln Pd\theta'd\varphi' \cdot \tau_i(\theta, \varphi, P_s \to 0) \quad (1)$$

where $B_i(T_i)$ is the observed TOA radiance for band i, T_i represents the band BT for band i observed at TOA, ε_i is the surface emissivity in band i, T_s is the surface temperature, $\tau_i(\theta, \varphi, P_s \to 0)$ is the total atmospheric transmittance
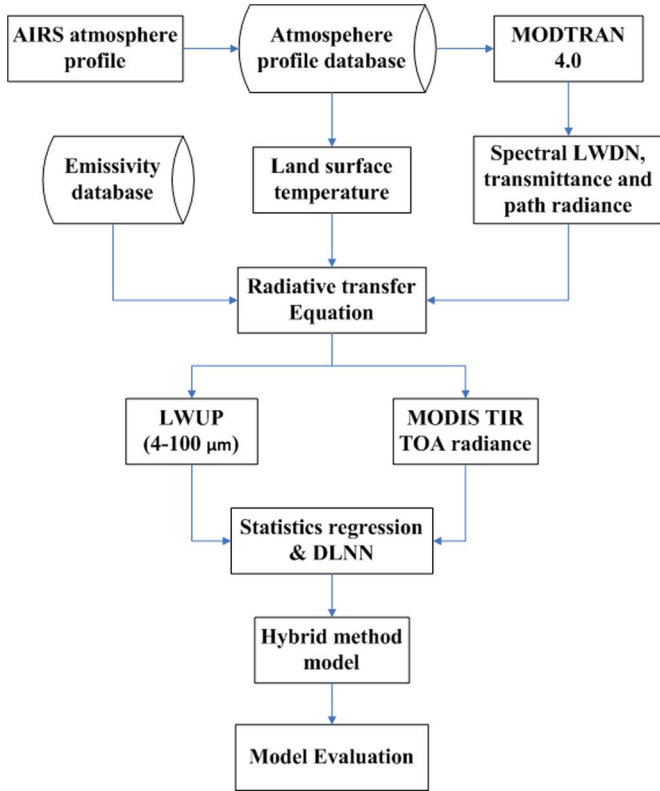
Fig. 2. Steps used to derive the hybrid method estimates.

along the target to sensor in band i, θ and φ are the viewing zenith angle and azimuth angle, P_s is the atmospheric pressure at ground level, T_p is the air temperature at the level of atmospheric pressure P, $\tau_i(\theta, \varphi, P \rightarrow 0)$ is the channel transmittance of the atmosphere from the level of atmospheric pressure P to the TOA, and $\tau_i(\theta, \varphi, P \rightarrow P_s)$ is the band transmittance of the atmosphere from the level of atmosphere pressure P to the ground level P_s. The first term on the right-hand side of (1) is the surface radiation, the second term denotes the sum of the radiance contributions from all of the atmospheric levels to the measured radiance, and the third term represents the hemispheric atmospheric downward longwave radiation reflected by the surface and then attenuated by the atmosphere along the path from the surface to the sensor. It is evident that the clear-sky TOA radiance contains information regarding the surface temperature, emissivity, and surface downward longwave radiation. The hybrid method derives the surface LWUP directly from the satellite TOA radiance or BT without separately estimating the three variables on the right-hand side of (1). This bypasses the problem of separating the LST and emissivity, resulting in a more accurate estimation of the surface upward longwave radiation. Fig. 2 shows the flowchart of deriving the hybrid method.

A. Radiative Transfer Modeling

The global land surface was divided into three subregions according to their latitudes, i.e., a low-latitude region ($0°-30°$ N, $0°-30°$ S), a midlatitude region ($30°-60°$ N, $30°-60°$ S),

and a high-latitude region ($60°-90°$ N, $60°-90°$ S). For each subregion, we first counted the total number of effective levels for each clear-sky atmosphere profile and then calculated the ratio of each total number from one year of AIRS L2 standard atmosphere products. This ratio was used as a reference to determine the ratio of atmosphere profiles with different effective levels in the constructed atmosphere profile database. For each total number, we constructed the initial atmosphere database and then updated the initial atmosphere database by comparing the new extracted atmosphere profile to those already in the initial atmosphere profile database. The following criteria [4] were used to determine the similarity of each new atmosphere profile to those already in the atmosphere profile database:

$$w_i = \frac{1}{z_i + 1} \tag{2}$$

$$S_T = \sum_{i=1}^{n} (w_i(T_{1,i} - T_{2,i})) \tag{3}$$

$$S_M = \sum_{i=1}^{n} (w_i|M_{1,i} - M_{2,i}|) \tag{4}$$

where z_i is the height of level i, w_i indicates the weight of height, S_T and S_M are the similarity in temperature and water vapor, $T_{1,i}$ and $T_{2,i}$ are the temperatures at altitude i for two temperature profiles, $M_{1,i}$ and $M_{2,i}$ are water vapor profiles at altitude I, and n is the total number of effective levels of an atmosphere profile. If the calculated S_T and S_M are both larger than set thresholds, e.g., 1.5 K and 300 ppmv, the new atmosphere profile was added to the atmosphere profile database; otherwise, it was excluded. In total, 41 724, 35 487, and 2842 atmosphere profiles were used in the construction of the low-latitude, midlatitude, and high-latitude region atmosphere profile databases, respectively. The Moderate Resolution Transmittance Code Version 4.0 (MODTRAN 4) [33] was used to simulate spectral LWDN, transmittance, and thermal path radiance for each atmosphere profile and was selected for its high computational efficiency and acceptable accuracy. The spectral transmittance and path thermal radiance were simulated at $0°$, $15°$, $30°$, $45°$, and $60°$ sensor view zenith angles.

To obtain the LST, we first calculated the difference between LST and temperature at the bottom layer using the atmosphere profile database for each subregion. The LST was then generated with the bottom layer temperature and the difference to cover the possible variation of actual LST. For example, the difference for the midlatitude region lies between -15 K and 20 K. The LST was assigned as the bottom layer temperature plus $[-15, 20]$ K, with a step of 5 K. Land surface emissivity was obtained from the Advanced Spaceborne Thermal Emission and Reflection Radiometer (ASTER) spectral library [34] and MODIS UCSB spectral library [35], [36]. Representative soil, vegetation, snow/ice, and water emissivity spectra were selected to construct the emissivity database. In addition, mixed pixels were also considered by area weighted average pure component emissivity spectra linearly. In total, 84 emissivity spectra representing various natural surfaces were used in this

TABLE II
SUMMARY OF THE FITTING RESULTS FOR LINEAR MODELS AND DLNN MODELS

Low-latitude region

	Linear model							DLNN		
θ	a_0	a_1	a_2	a_3	R^2	Bias	RMSE	R^2	Bias	RMSE
0°	118.807	-1.236	155.740	-126.281	0.991	0.00	7.87	0.996	0.00	5.47
15°	121.078	-1.182	158.025	-129.038	0.991	0.00	7.99	0.996	0.00	5.49
30°	128.588	-0.884	165.195	-137.861	0.990	0.00	8.46	0.996	0.00	5.71
45°	144.119	0.348	178.241	-154.825	0.988	0.00	9.51	0.995	0.00	6.24
60°	176.288	6.153	198.059	-185.369	0.979	0.00	12.31	0.992	0.00	7.76

Mid-latitude region

	Linear model							DLNN		
θ	a_0	a_1	a_2	a_3	R^2	Bias	RMSE	R^2	Bias	RMSE
0°	98.654	-1.460	138.154	-104.873	0.994	0.01	6.32	0.996	0.00	4.89
15°	100.396	-1.505	140.500	-107.528	0.994	0.01	6.42	0.996	0.00	4.96
30°	106.164	-1.566	147.916	-116.038	0.993	0.00	6.76	0.996	0.00	5.17
45°	118.150	-1.252	161.760	-132.508	0.991	0.00	7.47	0.995	0.00	5.66
60°	143.546	1.590	185.170	-163.217	0.987	0.00	9.33	0.993	0.00	6.80

High-latitude region

	Linear model							DLNN		
θ	a_0	a_1	a_2	a_3	R^2	Bias	RMSE	R^2	Bias	RMSE
0°	74.506	-6.201	114.816	-73.069	0.996	0.00	4.78	0.998	0.00	3.52
15°	48.974	4.817	18.136	20.384	0.999	0.00	1.76	0.998	0.00	1.45
30°	48.918	4.695	19.121	19.476	0.999	0.00	1.81	0.999	0.00	1.49
45°	48.897	4.442	21.289	17.455	0.999	0.00	1.93	0.999	0.00	1.57
60°	49.262	3.829	26.592	12.446	0.999	0.00	2.20	0.999	0.00	1.79

paper. The emissivity spectrum in the spectral region beyond the span of the spectral library was extrapolated from the original emissivity spectra. After we determined the surface and atmosphere parameters, the MODIS TOA channel radiances were synthesized based on the following simplified thermal infrared radiative transfer equation allowing the response functions of MODIS TIR channels:

$$L_i = \int_{\lambda_1}^{\lambda_2} \left(\left(\varepsilon_\lambda B(T_s) + (1 - \varepsilon_\lambda) L_{\downarrow_\lambda} \right) \tau_\lambda + L_{\uparrow_\lambda} \right) f_i(\lambda) d\lambda \quad (5)$$

where L_i is the MODIS TOA radiance for channels 29, 31, and 32, ε_λ is the emissivity spectra, $L_{\downarrow_\lambda}$ is the spectral LWDN, $L_{\uparrow_\lambda}$ is the thermal path radiance, $f_i(\lambda)$ is the response function for channels 29, 31, and 32, and λ_1 and λ_2 are the spectral range for a specific channel. LWUP can also be calculated using (5) with an integration range of 4–100 μm.

B. Linear Model

TOA radiances from MODIS channels 29, 31, and 32 were used to predict LWUP because of their sensitivity to LWUP

variations as well as the physics that govern LWUP. Multiple regression analysis was employed to develop a linear model, expressed as follows:

$$\text{LWUP} = a_0 + a_1 L_{29} + a_2 L_{31} + a_3 L_{32} \qquad (6)$$

where a_0, a_1, a_2, and a_3 are regression coefficients and L_{29}, L_{31}, and L_{32} are the TOA radiances for MODIS channels 29, 31, and 32, respectively. Statistical analysis indicated that the linear model accounts for more than 97.9%, 98.7%, and 99.6% of the variation in the simulated databases for the low-latitude, midlatitude, and high-latitude regions, respectively. Most of the biases are zero, and the RMSEs range from 7.87 to 12.31 W/m^2, 6.32 to 9.33 W/m^2, and 1.81 to 4.78 W/m^2 for the low-latitude, midlatitude, and high-latitude regions, respectively. Table II summarizes the fitting results of the linear models.

The effects of surface conditions and meteorological parameters on the accuracy of the LWUP estimate were also investigated. There is little correlation between the residuals (predicted LWUP minus true LWUP) and total column water, and the effect of total column water on the accuracy of the LWUP estimate is not significant. When the LST is extremely low, the LWUP is overestimated. In addition, no underestimated or overestimated trend is observed. The magnitude of BBE rather than vegetation cover should impact the accuracy of the LWUP estimate. However, no obvious underestimated or overestimated trend is observed.

C. DLNN Model

A neural network is an interconnection of simple computational elements, or nodes, with activation functions that are usually nonlinear, monotonically increasing, and differentiable [37]. Without any *a priori* knowledge of the data distribution and the relationship between the input variables and the output variables, a neural network can directly establish a relationship between the input variables and the output variables from the training ensembles. Furthermore, a neural network with only a single hidden layer of a sufficient number of nodes with nonlinear activation functions is capable of approximating any real-valued continuous scalar function to a given precision over a finite domain [38]. A neural network is therefore a powerful tool for solving nonlinear problems. Neural networks have been successfully applied to parameter inversion in remote sensing, such as atmospheric composition retrieval [37], [39], [40] and land surface parameter retrieval [41]–[50], which are strongly nonlinear problems. The dynamic learning neural network (DLNN) was actually a modified multilayer perceptron in structure, and the Kalman filtering technique was used in its learning process. By taking two modifications, we get the following results: 1) every node in the input layer and in all hidden layers was fully connected to the output layer, and 2) the activation function was removed from each output layer. The output of the modified network can be expressed by the weighted sum of the polynomial basis vectors [51]

$$\underline{y} = \underline{W}\,\underline{x} \qquad (7)$$

TABLE III
R^2 AND RMSE CORRESPONDING TO DIFFERENT
CONFIGURATIONS OF THE DLNN

Hidden layers	R^2	RMSE	Hidden Layers	R^2	RMSE
1	0.994	6.32	1-1	0.994	6.31
2	0.994	6.31	2-2	0.994	6.25
5	0.995	5.84	5-5	0.996	5.75
10	0.995	6.02	10-10	0.996	5.30
20	0.996	5.23	20-20	0.996	5.03
30	0.996	5.19	30-30	0.996	4.89
50	0.997	4.96	50-50	0.997	4.83
100	0.997	4.93	100-100	0.997	4.73
200	0.997	4.83	200-200	0.997	4.70

where $\underline{y}$ is the output vector, $\underline{x}$ is the vector that contains all input and hidden nodes, and the matrix $\underline{W}$ is formed by concatenating all the weights that are connected to output nodes. This linearization allowed the Kalman filtering algorithm to update the weights during the learning process. The DLNN updated the weights in a global manner, avoiding backpropagation, which usually makes the learning process very lengthy, and achieved fast learning. In addition, the DLNN had the features of global minimization, convergence warranty, and built-in optimization of a weighting function at little expense to computer storage [52].

To explore the nonlinearity between LWUP and TOA radiances, we also used the DLNN to establish the nonlinear relationship between LWUP and TOA radiances using the same samples as in Section III-B. The structure of the DLNN was determined by trail and test for each subregion. Table III gives the test results of $0°$ view zenith angle for the midlatitude region. The fitting results of the DLNN gradually improved with the increasing number of hidden layers and nodes, but the improvement was not significant. The accuracy of the DLNN with two hidden layers was better than with only one hidden layer. We can speculate that the fitting results of the DLNN will slowly improve with the increase of hidden nodes, but the computational cost will increase dramatically. For example, the number of coefficients exceeds 40 000 for the DLNN structure of 3-200-200-1. It is impractical to use such a network to retrieve LWUP at large scales. Therefore, the structure of the DLNN was set as 3-30-30-1 for each view zenith angle of each subregion in this paper. The performance of the DLNN is presented in Table II. Statistical analysis indicated that the DLNN model accounts for more than 99.2%, 99.3%, and 99.8% of the variation in the simulated databases for the low-latitude, midlatitude, and high-latitude regions, respectively. The biases of the DLNN models are zero, and the RMSEs range from 5.47 to 7.76 W/m^2, 4.89 to 6.80 W/m^2, and 1.45 to 3.52 W/m^2 for the low-latitude, midlatitude, and high-latitude regions, respectively. The bias and RMSE of DLNN models are slightly smaller than those of the linear models. The effects of surface conditions and meteorological parameters on the accuracy of LWUP estimation using the DLNN model are similar to that of the linear model.
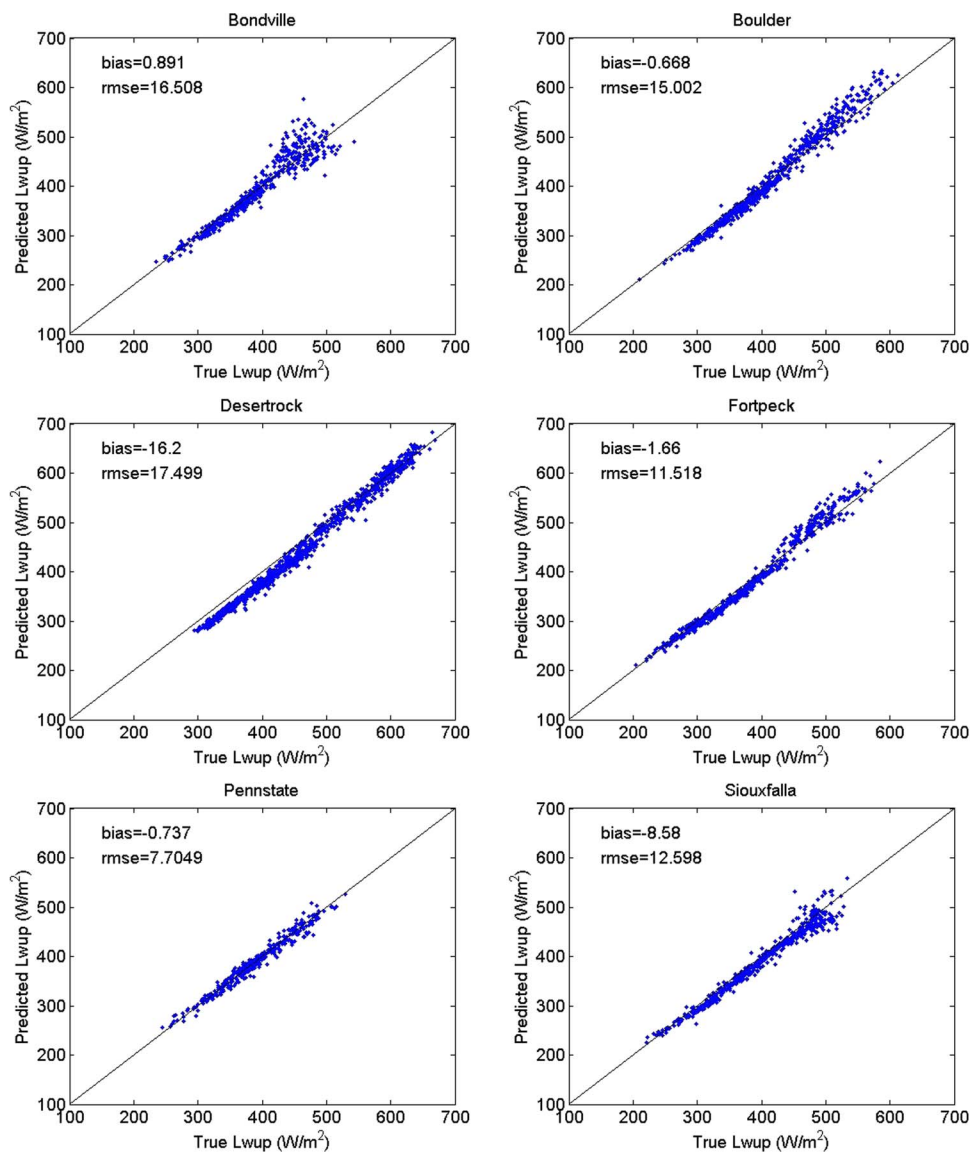
Fig. 3. Validation results of linear model using SURFRAD sites.

IV. VALIDATION AND DISCUSSION

A. Ground Measurements

The linear and DLNN models were validated using the ground-measured LWUP collected by three independent networks. The spectral range mismatch was not considered during the evaluation, as this error is less than 0.5% for surface temperatures between 240 and 330 K [12]. LWUP for different view zenith angles was linearly interpolated from those derived from the neighboring view zenith angles. When the view angle was larger than 60°, the model developed for the 60° view zenith angle was used. Clear-sky pixels were identified using the MODIS cloud mask product MOD35. Only clear-sky pixels at the highest confidence (99%) were considered. Figs. 2–8 show the validation results of the linear and DLNN models.

At the SURFRAD sites, the accuracy of the linear model is slightly better than that of the DLNN model, although the

performance of the latter is slightly better than that of the former using the training samples. The average bias and RMSE were −4.49 W/m² and 13.47 W/m² for the linear model and −5.60 W/m² and 16.17 W/m² for the DLNN model at the SURFRAD sites. Table III provides the statistical validation results for each site using the linear and DLNN methods. As shown in Figs. 3 and 4, there are some points with larger errors, even though the overall accuracy was acceptable. This is because of the following reasons. 1) The points are much more scattered in daytime than nighttime for both methods, as a result of the Earth's surface being more isothermal and homogeneous in nighttime than daytime [25]. 2) The Desertrock site has the largest bias and RMSE among all six sites for both methods. Wang *et al.* [12] noted that the cloud contamination may be a significant source of error, as air traffic out of Los Angeles produces many cirrus clouds over this site. Even though a series of spectral tests with multiple MODIS bands is used in the generation of MOD35,
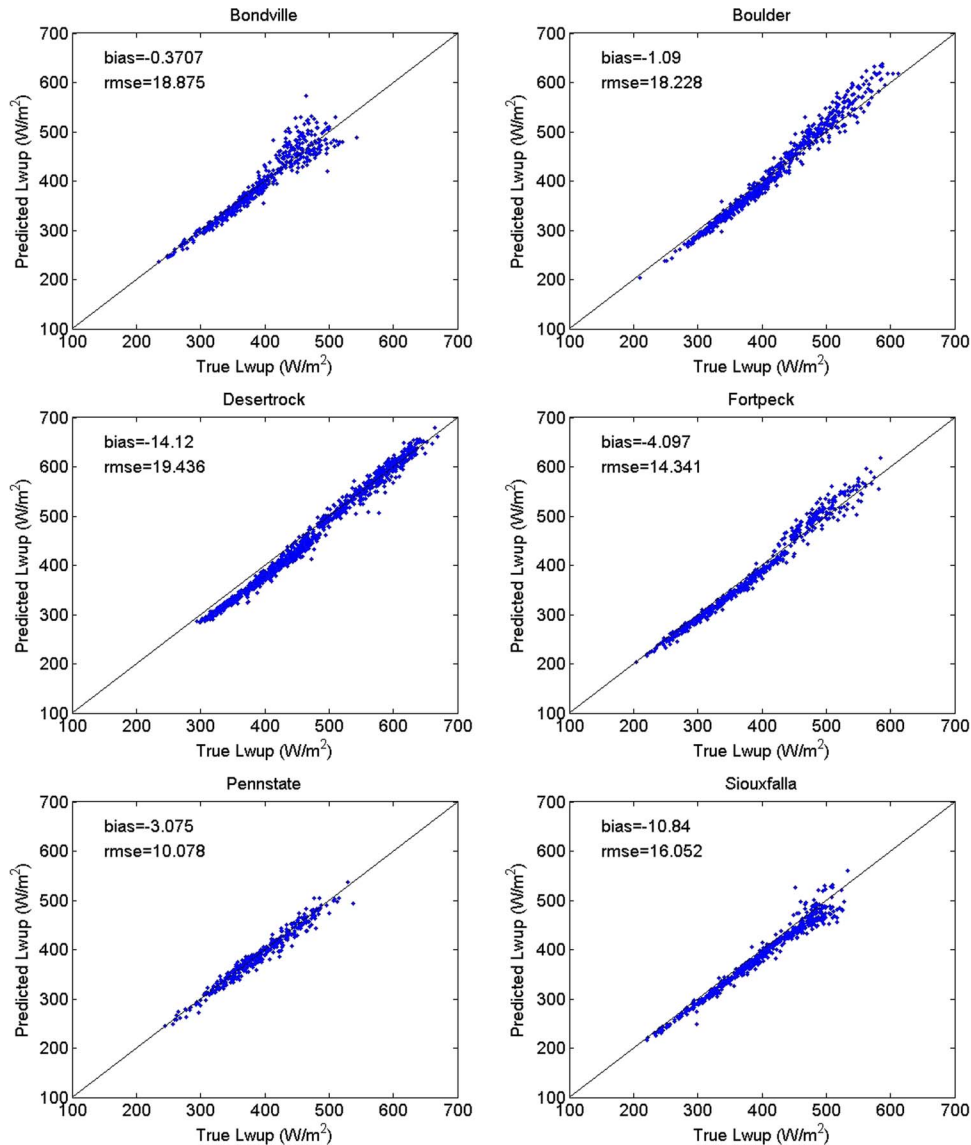
Fig. 4.   Validation results of DLNN model using SURFRAD sites.

it is impossible to make perfect cloud masking in all cases. Compared to the true clear-sky TOA radiance, the cloud contamination reduces the TOA radiance and the retrieved LWUP. 3) Finally, both methods underestimated the LWUP. The reason for this is highly complicated and difficult to identify. The measurement errors of satellites and pyranometers, angular effect of land surface and emissivity, scale mismatch, and error in the linear and DLNN models may contribute to this underestimation.

Similar to the validation results at SURFRAD sites, the accuracy of the linear model is slightly better than that of the DLNN model at ASRCOP sites. The average bias and RMSE were 1.06 W/m^2 and 17.61 W/m^2 for the linear model and -1.19 W/m^2 and 18.32 W/m^2 for the DLNN model at the ASRCOP sites. Table IV provides the validation results for each site using the linear and DLNN models. As shown in Figs. 5 and 6, there was not an obvious underestimation or overestimation trend. Regarding the GAME-AAN sites, we have

three sites in the low-latitude, midlatitude, and high-latitude regions. As shown in Table IV, the accuracy of the DLNN model is slightly better than that of the linear model. For the GAME-AAN sites, the average bias and RMSE were 2.49 W/m^2 and 28.67 W/m^2 for the linear model and 1.37 W/m^2 and 28.45 W/m^2 for the DLNN model. Accuracy at the high-elevation site Amdo was much better than at the other two sites. The number of acquired samples is quite limited for the latter two sites, and the points are also more scattered than that of the Amdo site (see Figs. 7 and 8).

According to the validation results, the linear model was superior to the DLNN model in this paper. The relatively complex structure of the DLNN model may explain why its performance was worse than the linear model when applied to real satellite measurements. The coefficients are over 1000 in the DLNN model, with a 3-30-30-1 network structure. There was no noise in the simulated data set. The DLNN model can incorporate the nonlinearity between LWUP and TOA
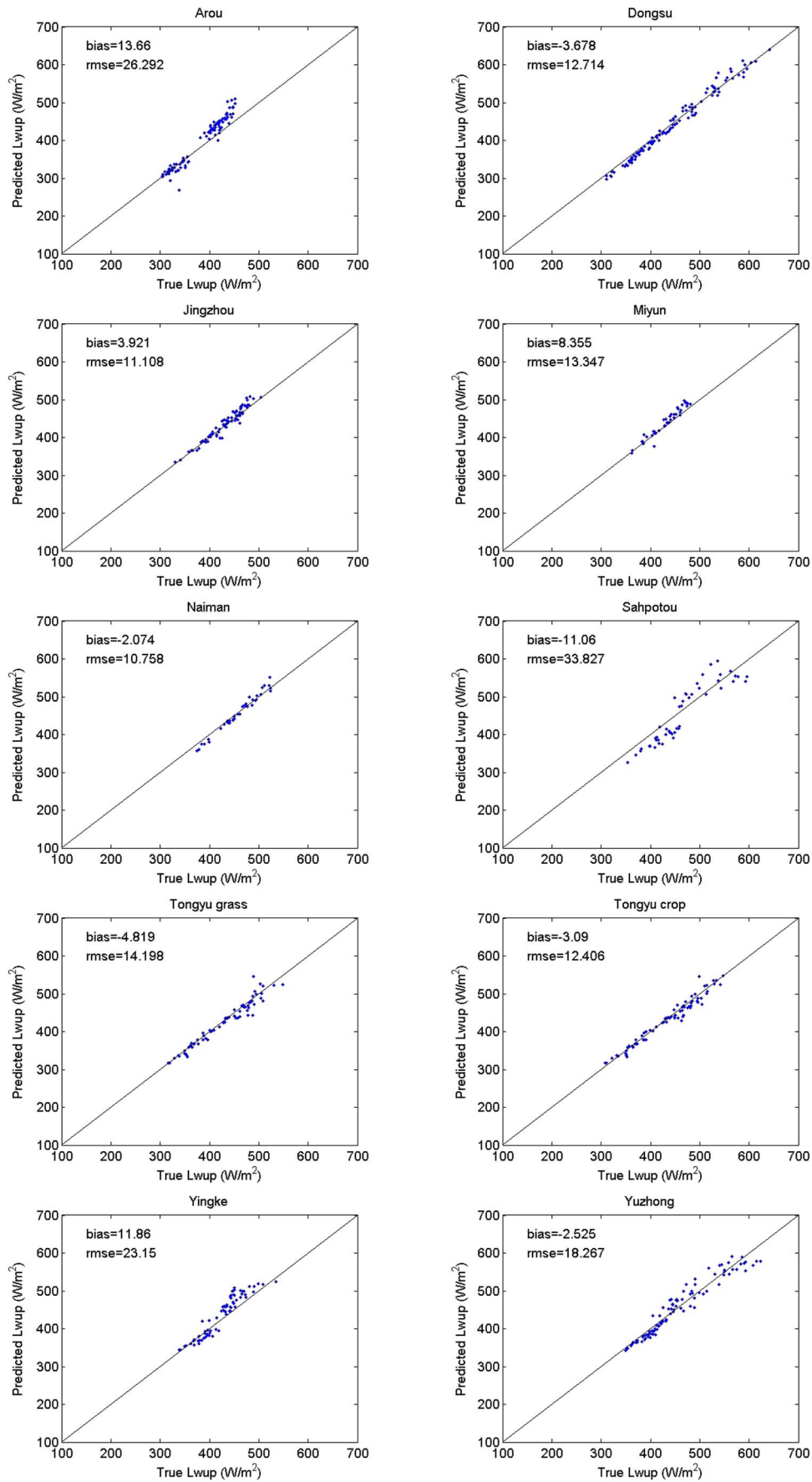
Fig. 5. Validation results of linear model using ASRCOP sites.
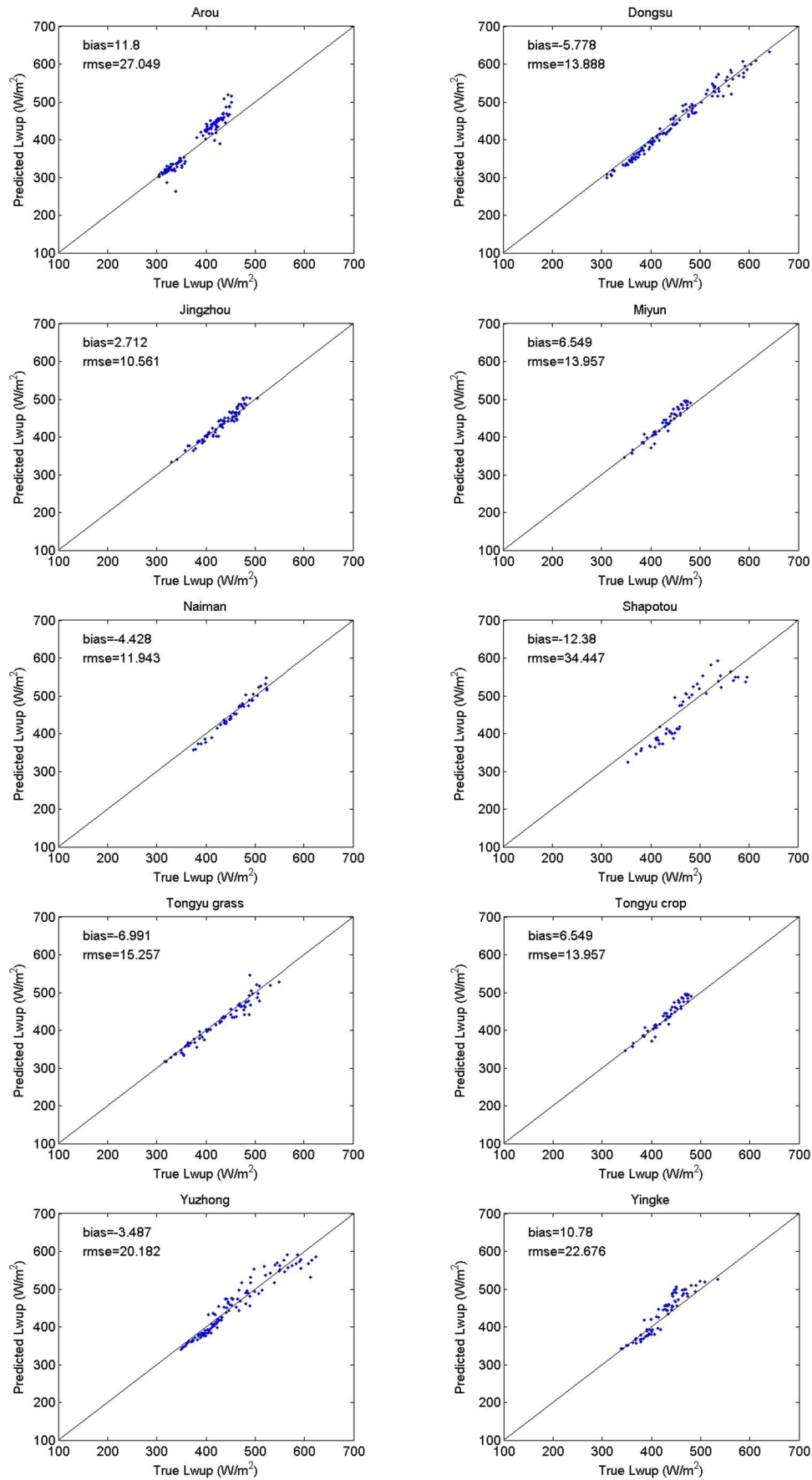
Fig. 6.   Validation results of DLNN model using ASRCOP sites.
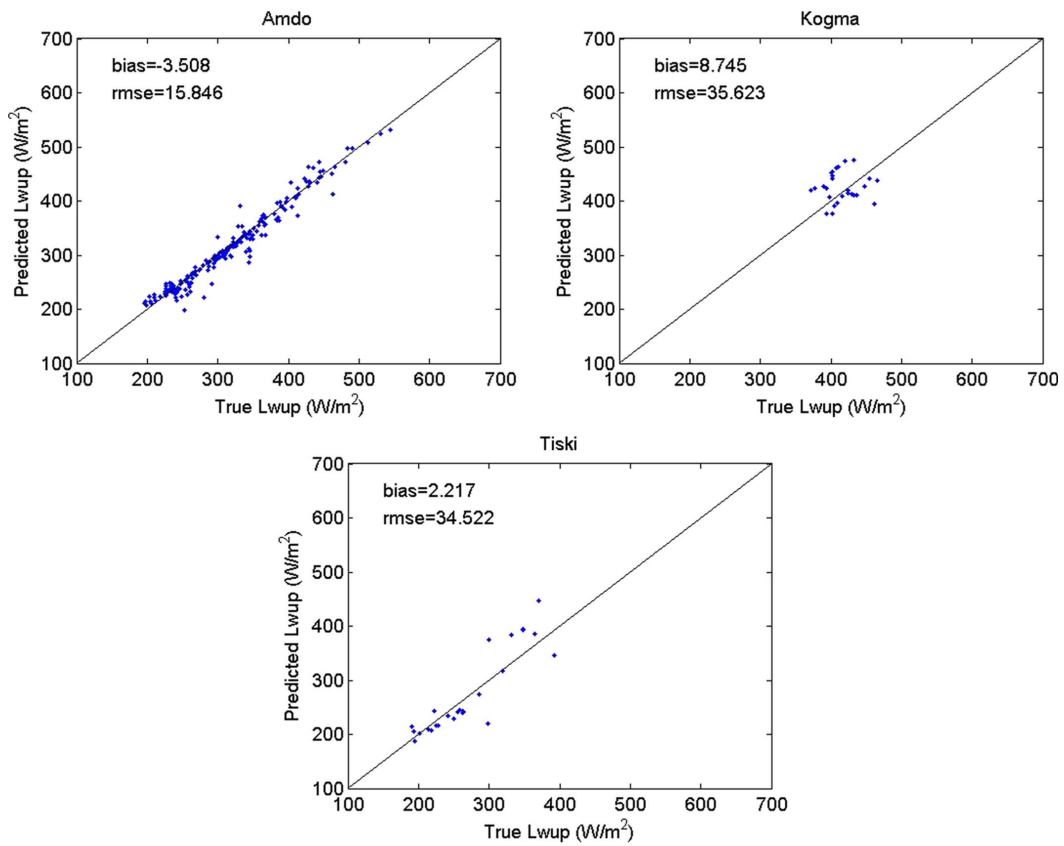
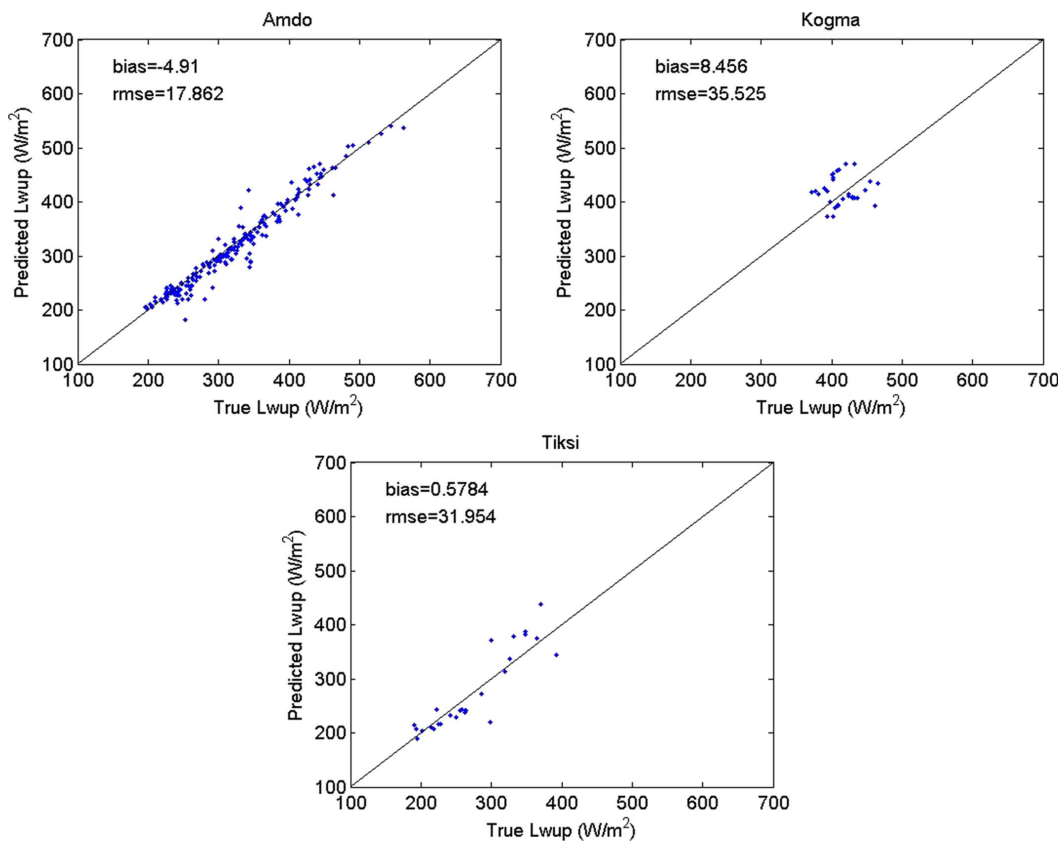Fig. 7. Validation results of linear model using GAME-AAN sites.

Fig. 8. Validation results of DLNN model using GAME-AAN sites.

TABLE IV
SUMMARY OF THE VALIDATION RESULTS AT ASRCOP AND GAME-AAN SITES USING MODIS TERRA DATA (UNIT: WATTS PER SQUARE METER)

Site Name	No. of Obs.	Linear Models		DLNN Models	
		Bias	RMSE	Bias	RMSE
ASRCOP					
Arou	148	13.66	26.29	11.8	27.05
Dongsu	122	-3.68	12.71	-5.78	13.89
Jingzhou	76	3.92	11.11	-2.71	10.56
Miyun	49	8.36	13.35	6.55	13.96
Naiman	41	-2.07	10.76	-4.43	11.94
Shapotou	51	-11.06	33.83	-12.38	34.45
Tongyu grass	71	-4.82	14.20	-6.99	15.26
Tongyu crop	77	-3.09	12.41	-5.26	13.18
Yingke	73	11.86	23.15	10.78	22.68
Yuzhong	113	-2.53	18.27	-3.49	20.18
Mean		1.06	17.61	-1.19	18.32
GAME-AAN					
Amdo	220	-3.51	15.85	-4.91	17.86
Kogma	32	8.75	35.62	8.46	35.53
Tiksi	28	2.22	34.52	0.58	31.95
Mean		2.49	28.67	1.37	28.45

TABLE V
SUMMARY OF THE VALIDATION RESULTS AT SURFRAD SITES USING MODIS TERRA DATA (UNIT: WATTS PER SQUARE METER)

Site Name	No. of Obs.	Linear Models		DLNN Models		Wang et al. Models	
		Bias	RMSE	Bias	RMSE	Bias	RMSE
Bondville	545	0.89	16.51	-0.37	18.88	-6.71	17.41
Boulder	683	-0.67	15.00	-1.09	18.23	-6.71	17.62
Desertrock	1192	-16.2	17.50	-14.12	19.44	-20.97	21.25
Fortpeck	616	-1.66	11.52	-4.10	14.34	-8.95	13.84
Pennstate	384	-0.74	7.70	-3.08	10.08	-8.21	10.21
Siouxfalla	583	-8.58	12.60	-10.84	16.05	-16.3	16.99
mean		-4.49	13.47	-5.60	16.17	-11.31	16.22

radiances and achieve a better accuracy than the linear model, but there are many types of errors in the satellite measurements. These errors are prone to be enlarged by the DLNN model as there are more than 1000 times the operations when the network structure is 3-30-30-1. Additionally, the computational efficiency of the linear model was higher than that of the DLNN model. There are four coefficients in the linear model. Therefore, the linear model was selected to estimate the global
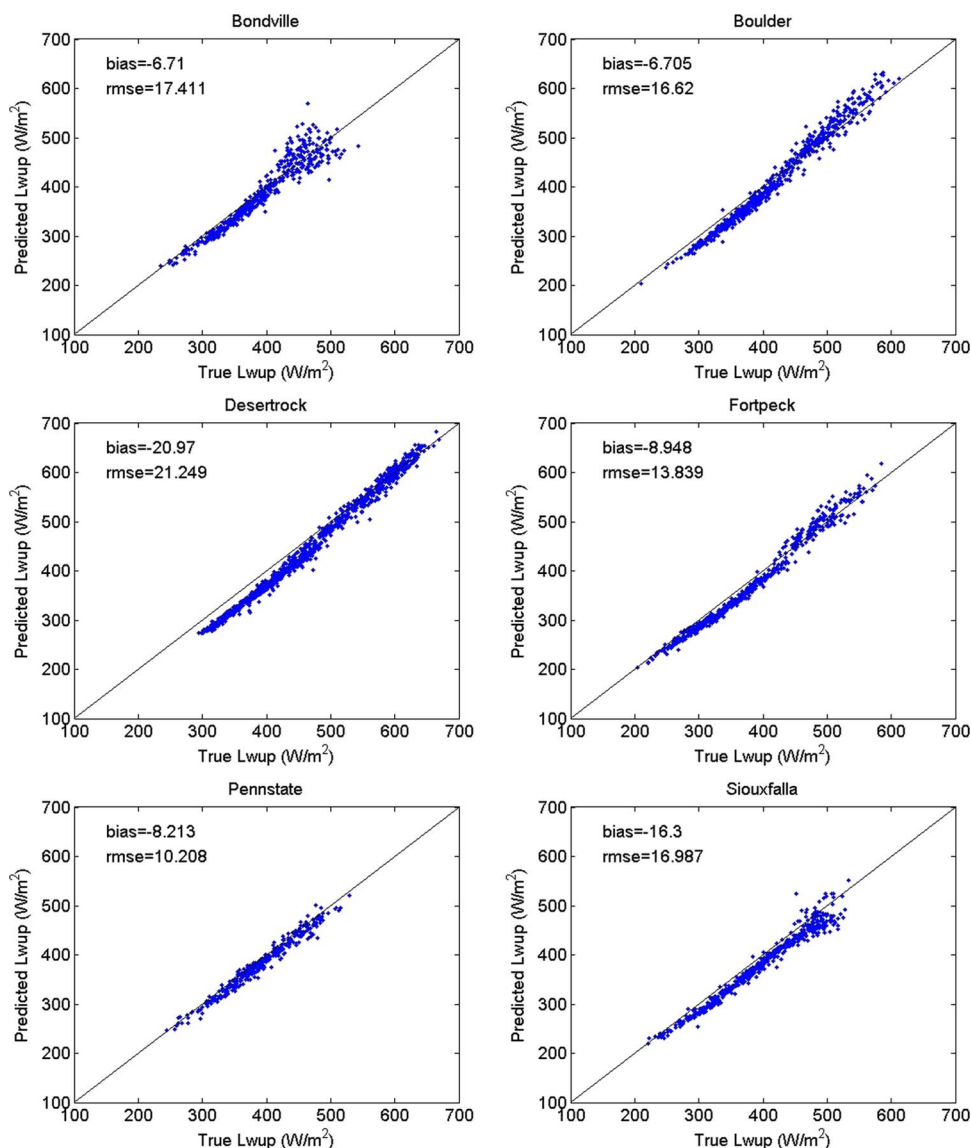
Fig. 9. Validation results of the Wang *et al.* linear model at SURFRAD sites.

1-km instantaneous clear-sky LWUP from the MODIS data in this paper.

B. Comparison With Previous Work

Wang *et al.* [12] developed the linear and artificial neural network (ANN) hybrid models for estimating North American LWUP using MODIS data. We validate their linear model with three years of SURFRAD measurements. The validation results are provided in Table V. The scatter distributions are very similar in Figs. 3 and 9. The accuracy of our linear method is better than the accuracy of the linear model of Wang *et al.* [12], the bias and RMSE of which were -16.31 W/m^2 and 16.22 W/m^2, respectively. We did not validate their ANN model, as we did not know the details of the information related to the used AAN. According to their validation using SURFRAD measurements in the years 2005–2006, the bias and RMSE were -8.67 W/m^2 and 15.89 W/m^2, respectively.

This accuracy is slightly worse that the accuracy of our linear model validated by three years of (2003–2005) SURFRAD measurements. Thus, our linear model performs better than the Wang *et al.* model in North America.

V. CONCLUSION

LWUP is a vital component for calculating the SRB. Under the general framework of the hybrid method, we developed the linear model and the DLNN model for estimating the global 1-km instantaneous clear-sky LWUP from the MODIS TOA radiance of channels 29, 31, and 32.

The global land surface was divided into three subregions according to their latitudes, i.e., low-latitude region ($0° - 30°$ N, $0° - 30°$ S), midlatitude region ($30° - 60°$ N, $30° - 60°$ S), and high-latitude region ($60° - 90°$ N, $60° - 90°$ S). For each sub-region, the AIRS standard L2 atmosphere profile products in 2008 and 2009 were used to construct the atmospheric profile

database. Spectral LWDN, thermal path radiance, and transmittance for each profile were simulated by MODTRAN4. Spectral path radiance and transmittance were simulated at $0°$, $15°$, $30°$, $45°$, and $60°$ sensor viewing zenith angles. LST was determined according to the bottom layer temperature of each atmosphere profile and the significant difference between bottom layer temperature and LST. Land surface emissivity was explicitly considered by incorporating the ASTER and MODIS UCSB spectral libraries in the radiative transfer simulation. In total, 84 emissivity spectra, including soil, vegetation, snow/ice, water, and some mixed scenarios, were used in this paper. Extensive radiative transfer simulations were conducted to produce a large number of representative samples, from which the linear and DLNN models were derived for each view zenith angle. Statistical analysis indicated that the linear model accounts for more than 97.9%, 98.7%, and 99.6% of the variation in the simulated databases for the low-latitude, midlatitude, and high-latitude regions, respectively. Most of the biases are zero, and the RMSEs range from 7.87 to 12.31 W/m^2, 6.32 to 9.33 W/m^2, and 1.81 to 4.78 W/m^2 for the low-latitude, midlatitude, and high-latitude regions, respectively. The DLNN model accounts for more than 99.2%, 99.3%, and 99.8% of the variation in the simulated databases for the low-latitude, midlatitude, and high-latitude regions, respectively. The biases of the DLNN models are zero, and the RMSEs range from 5.47 to 7.76 W/m^2, 4.89 to 6.80 W/m^2, and 1.45 to 3.52 W/m^2 for the low-latitude, midlatitude, and high-latitude regions, respectively. The biases and RMSEs of the DLNN models are slightly smaller than those of the linear models.

These two hybrid models were evaluated by the ground measurements collected at 19 sites from three networks (SURFRAD, ASRCOP, and GAME-AAN). The linear model was found to be superior to the DLNN model. The average bias and RMSE of the linear models were -4.49 W/m^2 and 13.47 W/m^2 at SURFRAD sites, 1.06 W/m^2 and 17.61 W/m^2 at ASRCOP sites, and 2.49 W/m^2 and 28.67 W/m^2 at GAME-AAN sites. Additionally, the computational efficiency of the linear model was higher than that of the DLNN model. Our linear model was also compared to the hybrid model developed by a previous study, which indicated that our linear model performs better than the latter. The linear model is being used to estimate the global 1-km instantaneous clear-sky LWUP products from 2010 to 2013.

REFERENCES

[1] S. Liang, K. Wang, X. Zhang, and M. Wild, "Review of estimation of land surface radiation and energy budgets from ground measurements, remote sensing and model simulation," *IEEE J. Sel. Topics Earth Observ. Remote Sens.*, vol. 3, no. 3, pp. 225–240, Sep. 2010.

[2] S. Liang, X. Zhang, T. He, J. Cheng, and D. Wang, "Remote sensing of land surface radiation budget," in *Remote Sensing of Land Surface Turbulent Fluxes and Soil Surface Moisture Content: State of Art*, G. P. Petropoulos, Ed. New York, NY, USA: Taylor & Francis, 2012.

[3] J. Cheng and S. Liang, "Effects of thermal-infrared emissivity directionality on surface broadband emissivity and longwave net radiation estimation," *IEEE Geosci. Remote Sens. Lett.*, vol. 11, no. 2, pp. 499–503, Feb. 2014.

[4] W. Wang, "Estimating high spatial resolution clear-sky land surface longwave radiation budget From MODIS and GOES data," Ph.D. dissertation, Dept. Geography, Univ. Maryland, College Park, MD, USA, 2008.

[5] S. Gui, S. Liang, and L. Li, "Evaluation of satellite-estimated surface longwave radiation using ground-based observations," *J. Geophys. Res.*, vol. 115, no. D18214, Sep. 2010, Art. no. D18214.

[6] "CEOS and WMO, CEOS/WMO online database: Satellite systems and requirements," Committee Earth Observ. Satellites, World Meteorol. Org., Geneva, Switzerland, 2000. [Online]. Available: http://192.91.247.60/sat/aspscripts/Requirementsearch.asp.

[7] S. K. Gupta, D. P. Kratz, and A. C. Wilber, "Validation of parameterized algorithms used to derive TRMM-CERES surface radiative fluxes," *J. Atmos. Ocean. Technol.*, vol. 21, no. 5, pp. 742–752, May 2004.

[8] V. Masson, J.-L. Chameraux, F. Chauvin, C. Meriguet, and R. Lacaze, "A global database of land surface parameters at 1-km resolution in meteorological and climate models," *J. Clim.*, vol. 16, no. 9, pp. 1261–1282, May 2003.

[9] O. B. Christensen and J. H. Christensen, "Very high-resolution regional climate simulations over Scandinavia-Present climate," *J. Clim.*, vol. 11, no. 12, pp. 3204–3229, Dec. 1998.

[10] S. Liang *et al.*, "Validating MODIS land surface reflectance and albedo products: Methods and preliminary results," *Remote Sens. Environ.*, vol. 83, no. 1/2, pp. 149–162, Nov. 2002.

[11] G. Bisht, V. Venturini, S. Islam, and L. Jiang, "Estimation of the net radiation using MODIS (Moderate Resolution Imaging Spectrometer) data for clear sky days," *Remote Sens. Environ.*, vol. 97, no. 1, pp. 52–67, Jul. 2005.

[12] W. Wang, S. Liang, and J. A. Augustine, "Estimating high spatial resolution clear-sky land surface upwelling longwave radiation from MODIS data," *IEEE Trans. Geosci. Remote Sens.*, vol. 47, no. 5, pp. 1559–1570, May 2009.

[13] Z. Wan and J. Dozier, "A generalized split-window algorithm for retrieving land-surface temperature form space," *IEEE Trans. Geosci. Remote Sens.*, vol. 34, no. 4, pp. 892–905, Jul. 1996.

[14] S. Liang *et al.*, "A long-term Global Land Surface Satellite (GLASS) data-set for environmental studies," *Int. J. Digit. Earth*, vol. 6, no. S1, pp. 5–33, Dec. 2013.

[15] J. Cheng and S. Liang, "A comparative study of three land surface broadband emissivity datasets from satellite data," *Remote Sens.*, vol. 6, no. 1, pp. 111–134, Dec. 2014.

[16] W. Wang and S. Liang, "A method for estimating clear-sky instantaneous land-surface longwave radiation with GOES sounder and GORE-R ABI data," *IEEE Geosci. Remote Sens. Lett.*, vol. 7, no. 4, pp. 708–712, Oct. 2010.

[17] B. Tang and Z. L. Li, "Estimation of instantaneous net surface longwave radiation from MODIS cloud-free data," *Remote Sens. Environ.*, vol. 112, no. 9, pp. 3482–3492, Sep. 2008.

[18] Y. Ma, L. Zhong, Y. Wang, and Z. Su, "Using NOAA/AVHRR data to determine regional net radiation and soil heat fluxes over the heterogeneous landscape of the Tibetau Plateau," *Int. J. Remote Sens.*, vol. 33, no. 15, pp. 4784–4795, Aug. 2012.

[19] K. Wang and S. Liang, "Evaluation of ASTER and MODIS land surface temperature and emissivity products using long-term surface longwave radiation observations at SURFRAD sites," *Remote Sens. Environ.*, vol. 113, no. 7, pp. 1556–1565, Jul. 2009.

[20] G. C. Hulley and S. J. Hook, "Intercomparison of versions 4, 4.1 and 5 of the MODIS land surface temperature and emissivity products and validation with laboratory measurements of sand samples from the Namib desert, Namibia," *Remote Sens. Environ.*, vol. 113, no. 6, pp. 1313–1318, Jun. 2009.

[21] J. Cheng, S. Liang, J. Wang, and X. Li, "A stepwise refining algorithm of temperature and emissivity separation for hyperspectral thermal infrared data," *IEEE Trans. Geosci. Remote Sens.*, vol. 48, no. 3, pp. 1588–1597, Mar. 2010.

[22] W. L. Smith and H. M. Wolfe, "Geostationary satellite sounder (VAS) observations of longwave radiation flux," presented at the Satellite

Systems Measure Radiation Budget Parameters Climate Change Signal, Igls, Austria, 1983.

[23] H.-T. Lee and R. G. Ellingson, "Development of a nonlinear statistical method for estimating the downward longwave radiation at the surface from satellite observations," *J. Atmos. Ocean. Technol.*, vol. 19, no. 10, pp. 1500–1515, Oct. 2002.

[24] H.-T. Lee, "Development of a statistical technique for estimating the downward longwave radiation at the surface from satellite observations," Ph.D. dissertation, Dept. Meteorol., Univ. Maryland, College Park, MD, USA, 1993.

[25] W. Wang, S. Liang, and T. Meyer, "Validating MODIS land surface temperature products using long-term nighttime ground measurements," *Remote Sens. Environ.*, vol. 112, no. 3, pp. 623–635, Mar. 2008.

[26] T. Wang, G. Yan, and L. Chen, "Consistent retrieval methods to estimate land surface shortwave and longwave radiative flux components under clear-sky conditions," *Remote Sens. Environ.*, vol. 124, pp. 61–71, Sep. 2012.

[27] H. Aumann, M. T. Chanhine, and C. Gautier, "AIRS/AMSU/HSB on the AQUA mission: Design, science objectives, data products, and processing systems," *IEEE Trans. Geosci. Remote Sens.*, vol. 41, no. 2, pp. 253–264, Feb. 2003.

[28] J. Susskind, C. D. Barnet, and J. M. Blaisdell, "Retrieval of atmospheric and surface parameters from AIRS/AMSU/HSB data in the presence of clouds," *IEEE Trans. Geosci. Remote Sens.*, vol. 41, no. 2, pp. 390–409, Feb. 2003.

[29] B. Albrecht and S. K. Cox, "Procedures for improving pyrgeometer performance," *J. Appl. Meteorol.*, vol. 16, no. 2, pp. 188–197, Feb. 1977.

[30] J. A. Augustine, J. J. DeLuisi, and C. N. Long, "SURFRAD—A national surface radiation budget network for atmospheric research," *Bull. Amer. Meteorol. Soc.*, vol. 81, no. 10, pp. 2341–2357, Oct. 2000.

[31] G. Huang et al., "Preliminary validation of GLASS-DSSR products using surface measurements collected in arid and semi-arid regions of China," *Int. J. Digit. Earth*, vol. 6, no. S1, pp. 50–68, Dec. 2013.

[32] S. M. Liu et al., "Measurements of evapotranspiration from eddy-covariance systems and large aperture scintillometers in the Hai River Basin, China," *J. Hydrol.*, vol. 487, pp. 24–38, Apr. 2013.

[33] A. Berk et al., *MODTRAN4 Version 3 Revision 1 User's Manual*. Bedford, MA, USA: Air Force Res. Lab., Hanscom Air Force Base, 2003.

[34] A. M. Baldridge, S. J. Hook, C. I. Grove, and G. Rivera, "The ASTER spectral library version 2.0," *Remote Sens. Environ.*, vol. 113, no. 4, pp. 711–715, Apr. 2009.

[35] W. C. Snyder, Z. Wan, Z. Zhang, and Y.-Z. feng, "Classification-based emissivity for land surface temperature measurement from space," *Int. J. Remote Sens.*, vol. 19, no. 14, pp. 2753–2774, Jan. 1998.

[36] W. C. Snyder and Z. Wan, "BRDF models to predict spectral reflectance and emissivity in the thermal infrared," *IEEE Trans. Geosci. Remote Sens.*, vol. 36, no. 1, pp. 214–225, Jan. 1998.

[37] W. J. Blackwell, "A neural-network technique for the retrieval of atmospheric temperature and moisture profiles from high spectral resolution sounding data," *IEEE Trans. Geosci. Remote Sens.*, vol. 43, no. 11, pp. 2535–2546, Nov. 2005.

[38] K. M. Hornik, M. Stinchcombe, and H. White, "Multilayer feedforward networks are universal approximators," *Neural Netw.*, vol. 4, no. 5, pp. 359–366, 1989.

[39] F. Aires, A. Chedin, N. A. Scott, and W. B. Rossow, "A regularized neural net approach for retrieval of atmospheric and surface temperatures with the IASI instrument," *J. Appl. Meteorol.*, vol. 41, no. 2, pp. 144–159, Feb. 2002.

[40] S. Turquety, J. Hadji-Lazaro, and C. Clerbaux, "First satellite ozone distributions retrieved from nadir high-resolution infrared spectra," *Geophys. Res. Lett.*, vol. 29, no. 24, pp. 51-1–51-4, Dec. 2002.

[41] J. Cheng, Q. Xiao, X. Li, Q.-H. Liu, and Y.-M. Du, "Multi-layer perceptron neural network based algorithm for simultaneous retrieving temperature and emissivity from hyperspectral FTIR data," *Spectrosc. Spectral Anal.*, vol. 28, no. 4, pp. 780–783, Apr. 2008.

[42] K. Mao et al., "A neural network technique for separating land surface emissivity and temperature from ASTER imagery," *IEEE Trans. Geosci. Remote Sens.*, vol. 46, no. 1, pp. 200–208, Jan. 2008.

[43] J. A. Smith, "LAI inversion using a back-propagation neural network trained with a multiple scattering model," *IEEE Trans. Geosci. Remote Sens.*, vol. 31, no. 5, pp. 1102–1106, Sep. 1993.

[44] H. Fang and S. Liang, "Retrieving leaf area index with a neural network method: Simulation and validation," *IEEE Trans. Geosci. Remote Sens.*, vol. 41, no. 9, pp. 2052–2062, Sep. 2003.

[45] Y. Jin and C. Liu, "Biomass retrieval from high-dimensional active/passive remote sensing data by using artificial neural network," *Int. J. Remote Sens.*, vol. 18, no. 4, pp. 971–979, Mar. 1997.

[46] L. Tang, Z. Chen, S. Oh, R. J. Marks, and A. T. C. Chang, "Inversion of snow parameters from passive microwave remote sensing measurements by a neural network trained with a multiple scattering model," *IEEE Trans. Geosci. Remote Sens.*, vol. 30, no. 5, pp. 1015–1024, Sep. 1992.

[47] M. Tedesco, J. Pulliainen, M. Takala, M. Hallikainen, and P. Pampaloni, "Artificial neural network-based techniques for the retrieval of SWE and snow depth from SSM/I data," *Remote Sens. Environ.*, vol. 90, no. 1, pp. 76–85, Mar. 2004.

[48] K. S. Chen, W. L. Kao, and Y. C. Tzeng, "Retrieval of surface parameters using dynamic learning neural network," *Int. J. Remote Sens.*, vol. 16, no. 5, pp. 801–809, Mar. 1995.

[49] F. Baret et al., "LAI, fPAR, and fCover CYCLOPES global products derived from VEGETATION. Part 1: Principles of the algorithm," *Remote Sens. Environ.*, vol. 110, no. 3, pp. 275–286, Oct. 2007.

[50] J. Cheng, S. Liang, Y. C. Tzeng, and L. Dong, "Obtaining global broadband emissivity from MODIS albedo product by using dynamic learning neural network," *Int. J. Remote Sens.*, vol. 35, no. 4, pp. 1395–1410, Feb. 2014.

[51] Y. C. Tzeng, K. S. Chen, W. L. Kao, and A. K. Fung, "A dynamic learning neural network for remote sensing applications," *IEEE Trans. Geosci. Remote Sens.*, vol. 32, no. 5, pp. 1096–1102, Sep. 1994.

[52] Y.-A. Liou, Y. C. Tzeng, and K. S. Chen, "A neural-network approach to radiometric sensing of land-surface parameters," *IEEE Trans. Geosci. Remote Sens.*, vol. 37, no. 6, pp. 2718–2724, Nov. 1999.

Jie Cheng (M'11) received the Ph.D. degree in cartography and remote sensing from the Institute of Remote Sensing Applications of the Chinese Academy of Sciences, Beijing, China, in 2008.

He was a Postdoctoral Fellow with the State Key Laboratory of Remote Sensing Science, Beijing Normal University, Beijing, from 2008 to 2010 and an Assistant Research Scientist with the University of Maryland, College Park, MD, USA, from 2009 to 2010. He is currently an Associate Professor with the State Key Laboratory of Remote Sensing Science, School of Geography, Beijing Normal University. His main research interests focus on the estimation of land surface variables from satellite observations, radiative transfer modeling, and studies on surface energy balance.

Shunlin Liang (M'94–F'13) received the Ph.D. degree from Boston University, Boston, MA, USA.

He is currently a Professor with the School of Geography, Beijing Normal University, Beijing, China, and the Department of Geographical Sciences, University of Maryland, College Park, MD, USA. His main research interests focus on the estimation of land surface variables from satellite data, earth energy balance, and assessment of environmental changes. He published over 220 SCI indexed journal papers, authored the book "Quantitative Remote Sensing of Land Surfaces"(Wiley, 2004), coauthored the book *Global LAnd Surface Satellite (GLASS) Products: Algorithms, Validation and Analysis* (Springer, 2013), edited the book *Advances in Land Remote Sensing: System, Modeling, Inversion and Application* (Springer, 2008), and coedited the books *Advanced Remote Sensing: Terrestrial Information Extraction and Applications* (Academic Press, 2012) and *Land Surface Observation, Modeling, Data Assimilation* (World Scientific, 2013).

Dr. Liang was an Associate Editor of the IEEE TRANSACTION ON GEOSCIENCE AND REMOTE SENSING and also a guest editor of several remote sensing-related journals.